Petroleum Science 20 (2023) 1104–1118

Contents lists available at ScienceDirect

Petroleum Science

journal homepage: www.keaipublishing.com/en/journals/petroleum-science

Original Paper

Structure optimization of the organ-pipe cavitating nozzle and its erosion ability test on hydrate-bearing sediments

Xiao-Ya Wu [a], Yi-Qun Zhang [b, c, *], Zhen-Qiang Xu [d, **], Shuai Zhao [b], Gen-Sheng Li [a, c], Shou-Ceng Tian [a], Ya-Wen Tan [a], Ke-Wen Peng [e]

[a] College of Petroleum Engineering, China University of Petroleum-Beijing, Beijing, 102249, China
[b] College of Safety and Ocean Engineering, China University of Petroleum-Beijing, Beijing, 102249, China
[c] State Key Laboratory of Natural Gas Hydrate, China University of Petroleum-Beijing, Beijing, 102249, China
[d] National Engineering Research Center of Gas Hydrate Exploration and Development, Guangzhou Marine Geological Survey, Guangzhou, 510075, Guangdong, China
[e] Guangdong Provincial Key Laboratory of Distributed Energy Systems, Dongguan University of Technology, Dongguan, 523808, Guangdong, China

ARTICLE INFO

Article history:
Received 10 May 2022
Received in revised form
14 October 2022
Accepted 17 October 2022
Available online 20 October 2022

Edited by Yan-Hua Sun

Keywords:
Natural gas hydrate
Cavitating jet
Structure optimization
Computational fluid dynamics
Experimental study

ABSTRACT

Cavitating jet is a promising drilling rate improvement technology in both the marine natural gas hydrate (NGH) fluidization exploitation method and the integrated radial jet drilling and completion method. In present study, we aim to improve the efficiency of jet erosion and extracting NGH. With a computational fluid dynamics (CFD) method, the pressure, velocity and cavitation field characteristics of organ-pipe cavitating jet (OPCJ) are analysed. The divergent angle, throat length, and divergent length of OPCJ nozzle are preferred to obtain stronger jet cavitation erosion effect. Laboratory experiments of gas hydrate-bearing sediments (GHBS) erosion by OPCJ and conical jet (CJ) are conducted to compare and validate the jet erosion performance. The impinging models of OPCJ and CJ are constructed to study the impact characteristics. Results show that the preferred values of divergent angle, throat length, and divergent length are 15°, 1*d*, and 3*d*, respectively, in present simulation conditions. For GHBS, the OPCJ possesses the advantages of high efficiency and low energy consumption. Moreover, the OPCJ has higher penetration efficiency, while showing equivalent penetration ability compared to CJ. During the impinging process, the OPCJ can induce stronger impact pressure and turbulence effect, and also shows stronger chambering effect and bottom cleaning ability compared to CJ. This study presents the erosion performance of OPCJ and CJ on GHBS, and provides preliminary insights on the potential field applications in NGH exploitation.

1. Introduction

Natural gas hydrate (NGH) is an ice-like crystalline compound formed by the combination of natural gas and water at low temperature and high pressure, which widely develops and exists in pores of earth, marine deep-water and plateau permafrost (Liang et al., 2022; Pang et al., 2022; Xu et al., 2022). The gas hydrate-bearing sediments (GHBS), as a large-scale efficient clean energy, have attracted much attention in the exploitation research (Zhang et al., 2022d).

At present, common recovery methods consist of depressurization, thermal stimulation, inhibitor injection and CO_2 replacement (Yu et al., 2019; Zhang et al., 2022c). Among these methods, depressurization is relatively feasible and widely adopted in field tests for its high efficiency and low cost (Shi et al., 2022; Terzariol et al., 2017; Yang et al., 2016; Zhang et al., 2022b). While there still exists the possibility that hydrate secondary formation blocks the flow path of NGH layers and restrict the long-term recovery (Circone et al., 2000). To meet the needs for safe, long-term, and economical exploitation of NGH reservoirs in the South China Sea, Zhou et al. (2014) proposed the solid fluidization mining method and successfully applied it to the field production test (Wang et al., 2017; Zhou et al., 2017). During this method, the water jet is a critical technology to crush GHBS into fine particles and the mixing slurry is transported upward to offshore platform for separation

* Corresponding author.
** Corresponding author.
E-mail addresses: zhangyq@cup.edu.cn (Y.-Q. Zhang), xzq17@aliyun.com (Z.-Q. Xu).

https://doi.org/10.1016/j.petsci.2022.10.010

and gas collection (Yang and Wang, 2019). Additionally, Li et al. (2020) proposed an innovative recovery mode of using a cavitating jet drilling radial wells and screen completion to extract NGH. This method utilizes the high efficiency and low energy consumption of cavitating jet, and can also combines the depressurization method to improve the recovery efficiency. In 2020, the horizontal well was adopted to develop NGH in the South China Sea and set a world record production of 2.87×10^4 m^3/day (Ye et al., 2020), which proved the feasibility of using horizontal well with depressurization.

The water jet erosion efficiency on GHBS is a key factor and attracts many studies. Chen et al. (2019a) studied the waterjet breaking efficiency on GHBS based the Arbitrary Lagrangian–Eulerian (ALE) method under various hydraulic conditions. Yang (2018) conducted simulation and experimental study to grasp the rules of jet velocity, standoff distance, and confining pressure on erosion effect of hydrate sediments by water jet and the hydraulic parameters were optimized. Wang et al. (2018) introduced a calculation principle to study the critical velocity of waterjet on GHBS, and experimental studies were conducted by Wang and Wang (2020) to optimize the waterjet parameters for improving erosion efficiency. Tang et al. (2020) designed a straight-swirling mixed nozzle and obtained the influence laws of operation conditions, nozzle number and NGH type on breaking efficiency. Zhang et al. (2021) studied the effects of jet time, standoff distance, jet pressure and horizontal section diameter on the crushing depth and volume based the non-diagenetic gas hydrate substitute samples. Yu et al. (2022) established a new model for predicting the hydrate breaking depth of single conical nozzle in solid fluidization method exploitation. Liao et al. (2022) investigated the impact of pressures, nozzle diameters and sand concentrations on slot shapes, morphologies and failure mode of natural gas hydrate to explore the applicability of hydraulic blasting technology. Zhang et al. (2022e) designed a swirling jet nozzle and studied the erosion effect on GHBS generated in laboratory compared to conical jet, and found that swirling jet can significantly increases the breaking efficiency.

Previous studies have proven that waterjet breaking technology is suitable for NGH reservoirs with non-diagenetic and weakly cemented seafloor. While the low breaking efficiency of conical jet (CJ) still restricts the economical recovery of hydrate resources. Additionally, most of the previous studies are conducted based on the hydrate substitute samples, which are different from GHBS in certain mechanical properties (Durham et al., 2003).

In the petroleum engineering and the ocean resource exploitation, the cavitating jets are widely used due to its stronger rock breaking ability compared to classical jet (Liao et al., 2020). Shen et al. (1991) developed a design method for organ-pipe cavitating nozzle and applied it in field drilling tests. It is demonstrated that the drill bits equipped with cavitating nozzles can improve the drilling rate by 2–4 times as compared with conventional nozzles. Therefore, in present study, the organ-pipe cavitating jet (OPCJ) is emphasized and the influences of nozzle structures, namely divergent angle, throat length and divergent length are analysed. Then, based on the visualization apparatus for NGH generation and water jet erosion, laboratory experiments of GHBS erosion by the OPCJ and CJ are conducted to validate the erosion performance of OPCJ. Finally, the impinging models are constructed to illustrate the impinging characteristics of the OPCJ and CJ. This study provides a OPCJ nozzle with high erosion efficiency for the NGH exploitation method using waterjet.

2. Methodology for simulation

2.1. Multiphase model

In present study, the organ-pipe cavitating jet is a turbulent flow in the vapor-liquid two-phase flow field, and the multiphase model, turbulence model and cavitation model are considered in the cavitating jet numerical simulation (Chen et al., 2019b). For the multiphase flow solutions, the single-fluid mixture model is appropriate to simulate cavitating vapor–liquid two-phase flows, which is capable of predicting the cavitation phenomena in water flows by solving a set of transport equations governing the mixture continuity, momentum, energy and the disperse phase for the volume fraction equation (Shi et al., 2019). The mixture model assumes that the velocities, temperature and densities of both the vapor and liquid phase are the same at every position in the two-phase fluid field (Chen et al., 2018). Additionally, the mixture model has the advantages of high accuracy, low resource occupancy and fast computational efficiency (Lei et al., 2015), so the mixture model is employed as the multiphase model in this study.

The mixture continuity equation can be expressed as,

$$\left.\begin{aligned} \frac{\partial}{\partial t}(\rho_{\mathrm{m}}) + \nabla\cdot(\rho_{\mathrm{m}}\boldsymbol{v}_{\mathrm{m}}) &= 0 \\ \boldsymbol{v}_{\mathrm{m}} &= \frac{\sum_{q=1}^{n}\alpha_q\rho_q\boldsymbol{v}_q}{\rho_{\mathrm{m}}} \\ \rho_{\mathrm{m}} &= \sum_{q=1}^{n}\alpha_q\rho_q \end{aligned}\right\} \tag{1}$$

where ρ_{m} is the density of the mixture phase; $\boldsymbol{v}_{\mathrm{m}}$ is the volume-averaged velocity of the mixture phase; α_q, ρ_q, and $\boldsymbol{v}_q$ represent the volume fraction, density and velocity of phase q (consisting of vapor and liquid phase), respectively.

The mixture momentum equations are defined as,

$$\left.\begin{aligned} \frac{\partial}{\partial t}(\rho_{\mathrm{m}}\boldsymbol{v}_{\mathrm{m}}) + \nabla\cdot(\rho_{\mathrm{m}}\boldsymbol{v}_{\mathrm{m}}\boldsymbol{v}_{\mathrm{m}}) &= -\nabla P + \nabla\cdot\left[\mu_{\mathrm{m}}\left(\nabla\boldsymbol{v}_{\mathrm{m}} + \nabla\boldsymbol{v}_{\mathrm{m}}^{\mathrm{T}}\right)\right] + \rho_{\mathrm{m}}\boldsymbol{g} + \boldsymbol{F} - \nabla\cdot\left(\sum_{q=1}^{n}\alpha_q\rho_q\boldsymbol{v}_{\mathrm{dr},q}\boldsymbol{v}_{\mathrm{dr},q}\right) \\ \mu_{\mathrm{m}} &= \sum_{q=1}^{n}\alpha_q\mu_q \end{aligned}\right\} \tag{2}$$

where P is the mixture pressure; μ_{m} is the viscosity of the mixture phase; μ_q is the viscosity of phase q (vapor and liquid phase); $\boldsymbol{g}$ is the gravitational acceleration; $\boldsymbol{F}$ is the body force; $\boldsymbol{v}_{\mathrm{dr},q}$ is the drift velocity of phase q; μ_{t} is the turbulence viscosity; u_i and u_j are the velocity in the i and j directions, respectively.

2.2. Turbulence model

The steady Reynolds-averaged Navier–Stokes (RANS) is widely used to solve the two-phase flows with turbulence effect, with its application range, computational accuracy and efficiency. Both the liquid and vapor phases are modelled using the Re-Normalization Group (RNG) $k-\varepsilon$ model (Yakhot and Orszag, 1986), which is verified by many studies that can get satisfactory results in the cavitating jet flow simulation (Cao et al., 2017; Celik et al., 2014; Yao et al., 2014). Therefore, the RNG $k-\varepsilon$ model is adopted to simulate the cavitating jet in present research.

The turbulent kinetic energy k and its dissipation rate ε are obtained from the following transport equations,

$$\frac{\partial(\rho k)}{\partial t}+\frac{\partial(\rho k u_i)}{\partial x_i}=\frac{\partial}{\partial x_j}\left[\alpha_k \mu_{\text{eff}}\frac{\partial k}{\partial x_j}\right]+G_k+\rho\varepsilon \tag{3}$$

$$\frac{\partial(\rho \varepsilon)}{\partial t}+\frac{\partial(\rho \varepsilon u_i)}{\partial x_i}=\frac{\partial}{\partial x_j}\left[\alpha_\varepsilon \mu_{\text{eff}}\frac{\partial \varepsilon}{\partial x_j}\right]+\frac{C_{1\varepsilon}^{*}\varepsilon}{k}G_k-C_{2\varepsilon}\rho\frac{\varepsilon^2}{k} \tag{4}$$

with

$$\left.\begin{aligned}
&\mu_{\text{eff}}=\mu+\mu_{\text{t}}\\
&\mu_{\text{t}}=\rho C_\mu\frac{k^2}{\varepsilon}\\
&C_\mu=0.0845,\alpha_k=\alpha_\varepsilon=1.39\\
&C_{1\varepsilon}^{*}=C_{1\varepsilon}-\frac{\eta(1-\eta/\eta_0)}{1+\beta\eta^3}\\
&C_{1\varepsilon}=1.42,C_{2\varepsilon}=1.68\\
&\eta=\left(2E_{ij}\cdot E_{ij}\right)^{1/2}\frac{k}{\varepsilon}\\
&E_{ij}=\frac{1}{2}\left(\frac{\partial u_i}{\partial x_j}+\frac{\partial u_j}{\partial x_i}\right)\\
&\eta_0=4.377,\beta=0.012
\end{aligned}\right\} \tag{5}$$

2.3. Cavitation model

The Schnerr–Sauer cavitation model is employed to calculate the phase transition between the water–liquid phase and the vapor phase (Schnerr and Sauer, 2001). This model is derived on the assumption of isothermal, incompressible and zero-slip velocity between the liquid phase and vapor phase (Shi et al., 2019). This model considers the positive mass transfer from the liquid phase to vapor phase and the Rayleigh–Plesset equation (Plesset, 1949; Rayleigh, 1917) is applied to describe the expansion of a single cavitation bubble in the liquid. Additionally, the Schnerr–Sauer model shows superiority in calculation accuracy and stability in previous work (Chen et al., 2019b; Lei et al., 2015; Wu et al., 2022).

The conservation equation for vapor volume fraction can be expressed as,

$$\left.\begin{aligned}
&\frac{\partial}{\partial t}(\alpha_{\text{v}}\rho_{\text{v}})+\nabla\cdot(\alpha_{\text{v}}\rho_{\text{v}}\boldsymbol{v}_{\text{m}})=S_{\text{e}}-S_{\text{c}}\\
&\alpha_{\text{v}}=\frac{n_{\text{b}}\frac{4}{3}\pi R_{\text{b}}^3}{1+n_{\text{b}}\frac{4}{3}\pi R_{\text{b}}^3}
\end{aligned}\right\} \tag{6}$$

where the source terms S_{e} and S_{c} represent the evaporation and condensation of vapor bubbles, respectively; the vapor volume fraction α_{v} is defined as a function of the number of spherical bubbles per volume of liquid n_{b} and the radius of bubble R_{b}.

The source terms S_{e} and S_{c} derived from Eq. (6) can be obtained as,

$$S_{\text{e}}=\frac{\rho_{\text{v}}\rho_{\text{l}}}{\rho_{\text{m}}}\alpha_{\text{v}}(1-\alpha_{\text{v}})\frac{3}{R_{\text{b}}}\sqrt{\frac{2(P_{\text{v}}-P_\infty)}{3\rho_{\text{l}}}},\ \text{for}\ P_{\text{v}}\geq P_\infty \tag{7}$$

$$S_{\text{c}}=\frac{\rho_{\text{v}}\rho_{\text{l}}}{\rho_{\text{m}}}\alpha_{\text{v}}(1-\alpha_{\text{v}})\frac{3}{R}\sqrt{\frac{2(P_\infty-P_{\text{v}})}{3\rho_{\text{l}}}},\ \text{for}\ P_{\text{v}}\leq P_\infty \tag{8}$$

$$R_{\text{b}}=\left(\frac{\alpha_{\text{v}}}{1-\alpha_{\text{v}}}\frac{3}{4\pi n_{\text{b}}}\right)^{1/3} \tag{9}$$

where the P_{v} is the saturation vapor pressure; P_∞ is the local-far field pressure; n_{b} is assumed to be 10^{13} in present study, which is also the optimal value proven in previous work (Li et al., 2008; Liu et al., 2013).

3. Computation setup

3.1. Problem description and geometry model

In current study, we emphasize the organ-pipe cavitating jet and the nozzle geometry configuration is shown in Fig. 1. The nozzle is composed of resonator and outlet structures. The key parameters of resonator consist of D_{s}, D, d and L, which represent the inlet diameter, resonator diameter, throat diameter and resonator length, respectively. For outlet structure, the important parameters mainly include θ, L_1 and L_2, which correspond to the divergent angle, throat length and divergent length. The specifications of organ-pipe cavitating nozzle are displayed in Table 1. The design of resonator refers to the previous work (Li and Shen, 1987, 1992) and the three parameters of outlet structure are selected as design variables.

3.2. Computational domain and solution strategy

Fig. 2 shows the 2D axisymmetric computational model used in this study. The length and width of the outflow field are set as 20d and 10d, respectively, to eliminate the influence of flow field boundary on the simulation results and allow the jet to fully develop (Zhang et al., 2000). Fig. 3 shows the computational domain discretized with block-structured (hexahedral) meshes using a finite-volume method. Considering that the flow characteristics in the throat and divergent section are more active, we

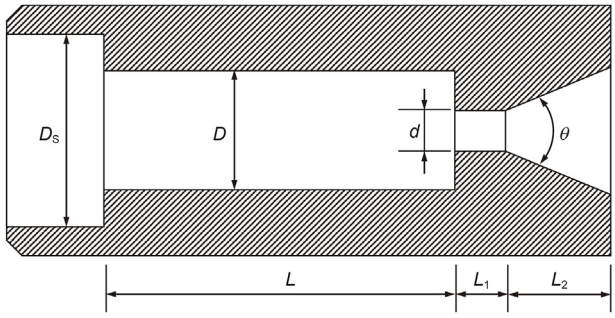

Fig. 1. Organ-pipe cavitating nozzle geometry.

Table 1
Specifications of organ-pipe cavitating nozzle.

Resonator structure							Outlet structure		
D_s, mm	D, mm	L, mm	d, mm	$(D_s/D)^2$	$(D/d)^2$	L/d	θ, degree	L_1/d	L_2/d
13	5	21	2	6.76	6.25	10.50	10/15/20/25/30	2	5
							20	1/2/3/4/5	5
							20	1	1/2/3/4/5/6/7

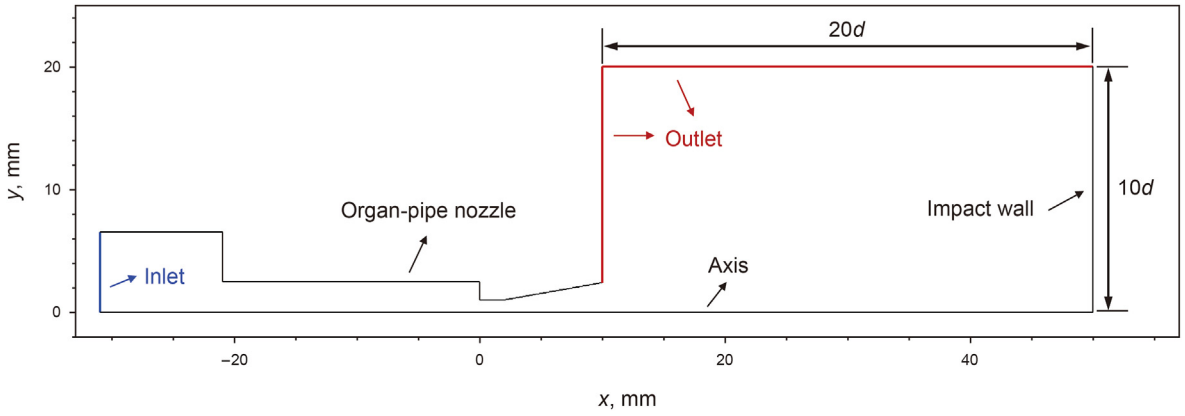

Fig. 2. The two-dimensional axisymmetric computational domain.

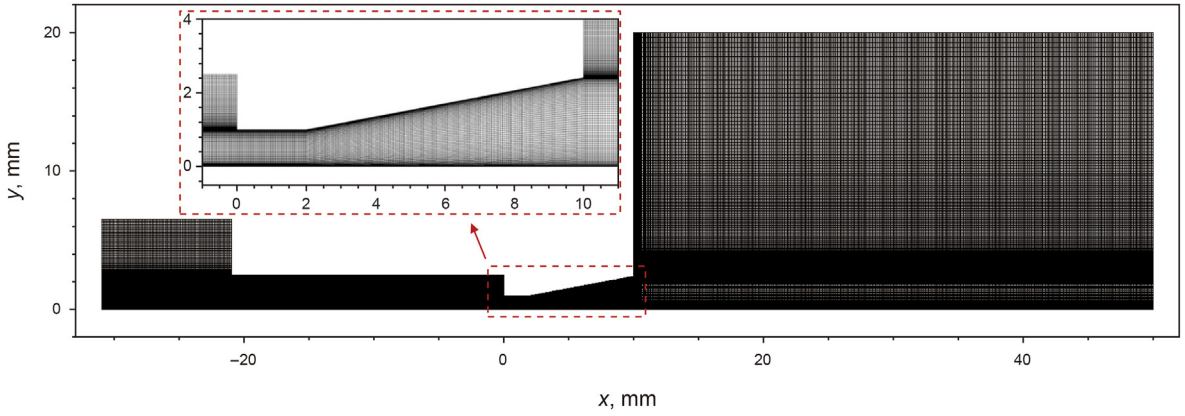

Fig. 3. The mesh of computational domain and local region.

refined mesh in this region to improve the calculation accuracy. Additionally, the average orthogonal quality of the mesh model is over 0.99 (1 is the best), which is of good quality for the application of CFD numerical simulation (Wang and Hu, 2015).

In all numerical models, the velocity inlet condition is applied at nozzle' inlet (blue line), with a constant value of 2.5 m/s. The pressure and temperature conditions are consistent with the settings in experiments described in Section 5.1. The pressure outlet condition is employed at nozzle's outlet (red line) and set to 5 MPa. The boundary conditions for turbulence are specified as possessing a uniform value of 10% for the turbulence intensity and 10 for the turbulent viscosity ratio (Shi et al., 2019). The non-slip boundary condition is applied at other walls. The saturation vapor pressure P_v is constant and set to 810 Pa. The saturation vapor pressure is calculated based on the Antoine equation (Thomson, 1946) as follows,

$$\log P_v = A - \frac{B}{T + C} \tag{10}$$

where P_v is the saturation vapor pressure of the water; T is the temperature of the water; A, B, and C are substance-specific coefficients and equal to 8.07131, 1730.63, and 233.426, respectively, when $1\ ^\circ C \leq T < 100\ ^\circ C$.

All the simulations are conducted using the CFD code ANSYS FLUENT 19.0. and performed based on steady-state conditions. The pressure-velocity-based coupled scheme is employed to solve the mass and momentum conservation equations, which corresponds to the behaviour of cavitating jet flow in the mixture model. The implicit discretization of the pressure gradient terms and the face mass flux are included in the equation to fulfil the coupling algorithms. The quadratic upwind interpolation for convection kinematics (QUICK) scheme is applied to discretize convective terms in the transport equation for the volume fraction of vapor. The

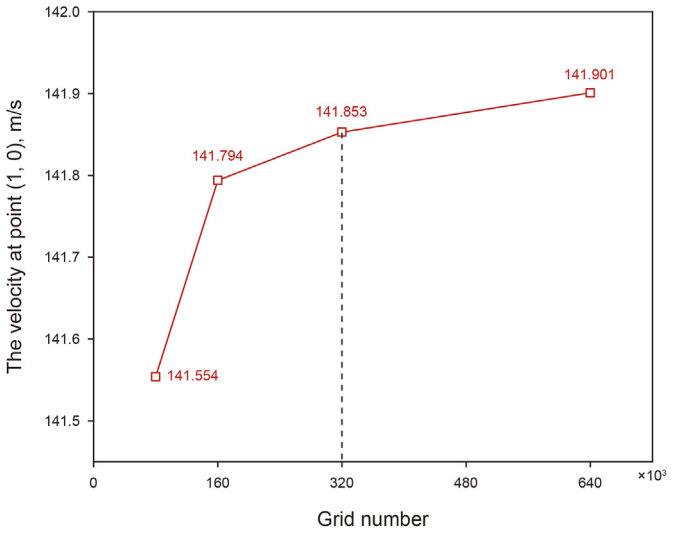

Fig. 4. The indicator velocity with different grid numbers.

pressure is discretized by using the PRESTO scheme considering that the flow field tends to generate a steep pressure gradient at the cell face. The second-upwind scheme is employed to discretize the convection terms in the momentum equations and the RANS model.

3.3. Grid independence study and model validation

To eliminate the effect of grid number, the influence of the grid resolution is studied to select an appropriate grid number for the simulations. The investigations were carried out based on the computational model shown in Fig. 3. The four groups of models with grid number of 80,000, 160,000, 320,000 and 640,000 are constructed and with same settings as shown in Section 3.3. The velocity at point (1, 0) was calculated as the indicator. It can be seen from Fig. 4 that the indicator velocity presents a negligible deviation of 0.03% when the grid number increases from 320,000 to 640,000. Therefore, it was decided that the grid number varying from 320.000 to 640,000 is employed for the rest of computational models.

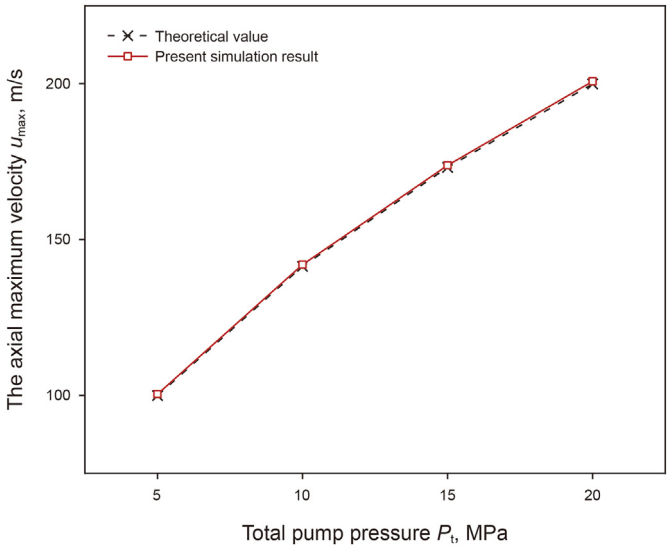

Fig. 5. The comparison of u_{max} between the theoretical and simulated results with different inlet pressures.

Based on this, we performed the model validation at different inlet pressures. The axial maximum velocities simulated with inlet pressures of 5, 10, 15, and 20 MPa are obtained, and the theoretical maximum jet velocities under same inlet conditions are calculated on the basis of equation $u_{max} = 44.7\sqrt{P_t}$ (Xue, 2006), where P_t represents the total pump pressure. The error value is defined as $\sigma = (u_{max,s} - u_{max,t})/u_{max,t}$, where $u_{max,s}$ and $u_{max,t}$ represent the simulated and theoretical values of u_{max}, respectively. From Fig. 5, it can be seen that the trend of $u_{max,s}$ and $u_{max,t}$ remains consistent with the variation of inlet pressure, and the σ calculated at different inlet pressures are both within 0.4% deviation. Additionally, the transient solution is employed to obtain the variation of cavitation clouds with time, the results of which are compared with experimental results, as shown in Fig. 6. Fig. 6a shows the morphological changes of cavitation clouds in a single cycle. Region A shows the cavitation initiation, and line B indicates the location of the separation of the cavitation cloud. In region C, all the bubbles collapse. Fig. 6b shows the simulation results of cavitation clouds with time and the variation trend agrees with that of Fig. 6a well, and the only difference is the definition of the initial time. As described by Tan et al. (2022), the migration velocities of the cavitation clouds at $t = 150$ μs and $t = 350$ μs are 50 and 30 m/s, respectively, and are consistent with the simulated velocities shown in Fig. 6c. Therefore, we conclude the simulation method adopted is feasible.

4. Simulation results and analyses

In all simulations, the inlet velocity condition is set to 2.5 m/s and the outlet pressure is set to 5 MPa. The influences of divergent angle, throat length and divergent length on pressure field, velocity field and cavitation field are analysed.

4.1. Influence of divergent angle on flow field

Fig. 7a shows the axial pressure distribution at different divergent angles (θ). All lines present similar distribution law. With the axial distance increases, the pressure reaches its maximum at the beginning, then drops to the minimum, and finally reaches to outlet pressure. The minimum pressure increase gradually as the θ increases. For θ varying from 10° to 30°, there exists large negative pressure zone in the throat. When the θ increases from 40° to 50°, the axial minimum pressure becomes positive. According to Brennen (2013), cavitation, by definition, is the process by which vapor bubbles forming and growing in a liquid when the local static pressure falls below the vapor pressure at a constant ambient temperature. Therefore, the jet generating greater negative pressure possesses the stronger cavitation inception ability. Additionally, the fluid in negative pressure zone is stretched, and greater negative pressure is more conducive to the formation of large size cavitation bubbles. By contrast, the nozzle with $\theta = 10°$ shows the best cavitation initiation ability. Jet velocity field mainly affects the migration of cavitation clouds. From Fig. 7b, as the θ increases, the jet potential core is more likely to form in the flow field.

Fig. 8a shows the distribution of cavitation clouds of divergent angles varying from 10° to 30°, and the cases with divergent angles of 40° and 50° are not displayed due to serious collapse of cavitation clouds. As the θ increases, the area of cavitation clouds increases first and then decreases gradually. When $\theta = 15°$, the area value of cavitation clouds is the greatest. The vapor volume fraction at walls of nozzle throat and divergent section is extracted as shown in Fig. 8b. The vapor volume fraction and distribution of nozzle with $\theta = 15°$ is greater than other nozzles especially when x

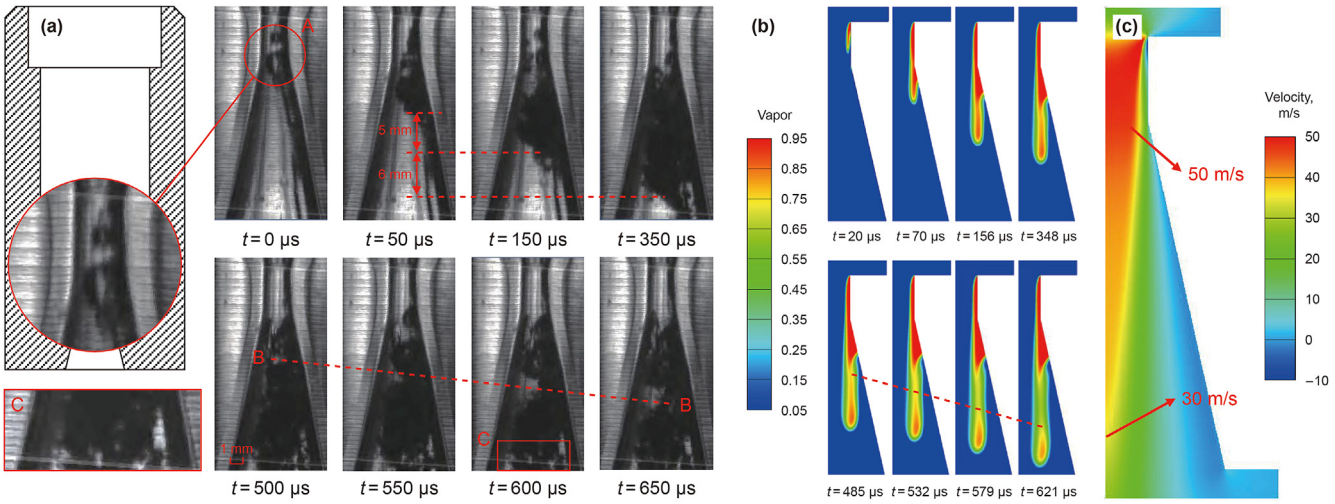

Fig. 6. A comparison between experimental and simulation results. (**a**) Morphological changes of cavitation clouds in a single cycle (Tan et al., 2022); (**b**) The variation of cavitation clouds with time; (**c**) Velocity contour.

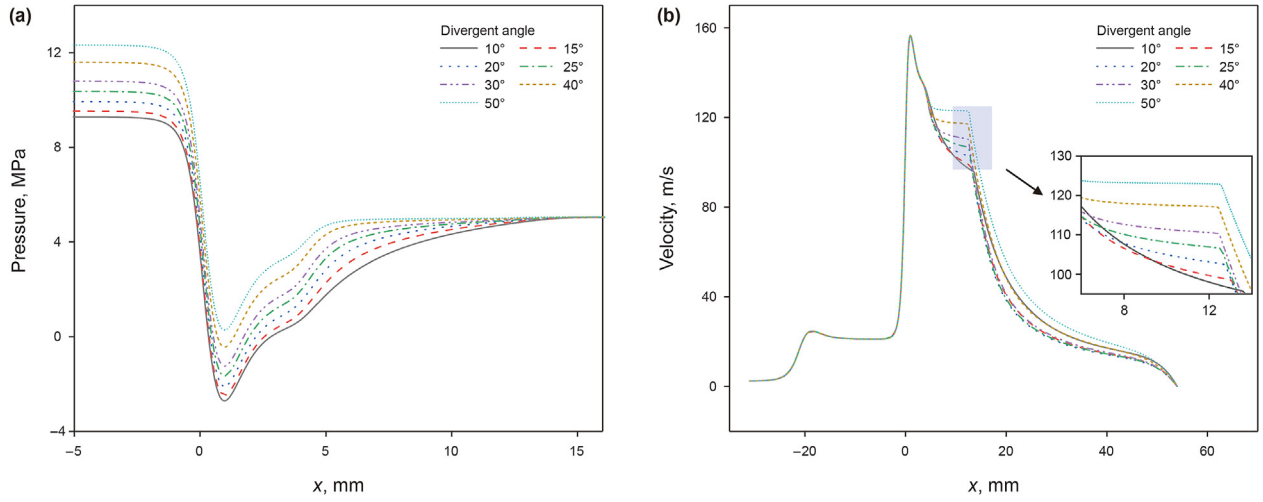

Fig. 7. A comparison of axial flow field characteristics. (**a**) Pressure distribution; (**b**) Velocity distribution.

exceeds 4 mm. It can be seen that the cavitation generates at the beginning of the throat and rapidly develops to the maximum vapor volume fraction. In the process of migration in the throat, the cavitation clouds collapse corresponding to the contours shown in Fig. 8a, and the vapor volume fraction decreases. While the vapor volume fraction increases significantly at the divergent section. This is because there exists velocity gradient between the high-speed fluid flowing out from the throat and the static fluid in the divergent section, and the existence of velocity gradient forms a shear effect and promotes the generation of vortex, as shown in Fig. 9. The characteristics of low pressure in vortex core promote the formation of cavitation. Additionally, at the end of cavitation clouds, the collapse behavior becomes violent with the θ increases shown in Fig. 8a. According to previous work (Kawanami et al., 1997; Mathieu et al., 2001; Wang et al., 2012), this phenomenon is generally attributed to the reverse jet generated at the shedding position, as shown in Fig. 9. The impact between the reverse jet and the main jet leads to the separation of the cavitation cloud from the divergent section, and the large-scale shedding of the cavitation clouds will occur as the fluid flows toward the outflow field. From Fig. 9, when the θ increases from 10° to 15°, the vortex develops and the vortex cavitation is strengthened. As the θ continuously increases from 15° to 30°, the impact effect between reverse jet and main jet becomes intense gradually, which causes that the shedding position of cavitation clouds advances. Especially at $\theta = 30°$, it can be seen from Fig. 9 the impact position between reverse and main jet is almost at the beginning of divergent section, which corresponds to the shedding position of cavitation clouds in Fig. 8a and b.

4.2. Influence of throat length on flow field

Fig. 10a shows the axial pressure distribution at different throat lengths (L_1). It can be seen that as the L_1 has slight influence on the axial minimum pressure, namely negative pressure zone. As L_1 increases, though the constant pressure zone is formed, the pressure value is positive and not conducive to the development of cavitation clouds. From Fig. 10b, increasing L_1 promotes the formation of jet potential core and is conducive to the migration of cavitation clouds, especially when $L_1 = 5d$.

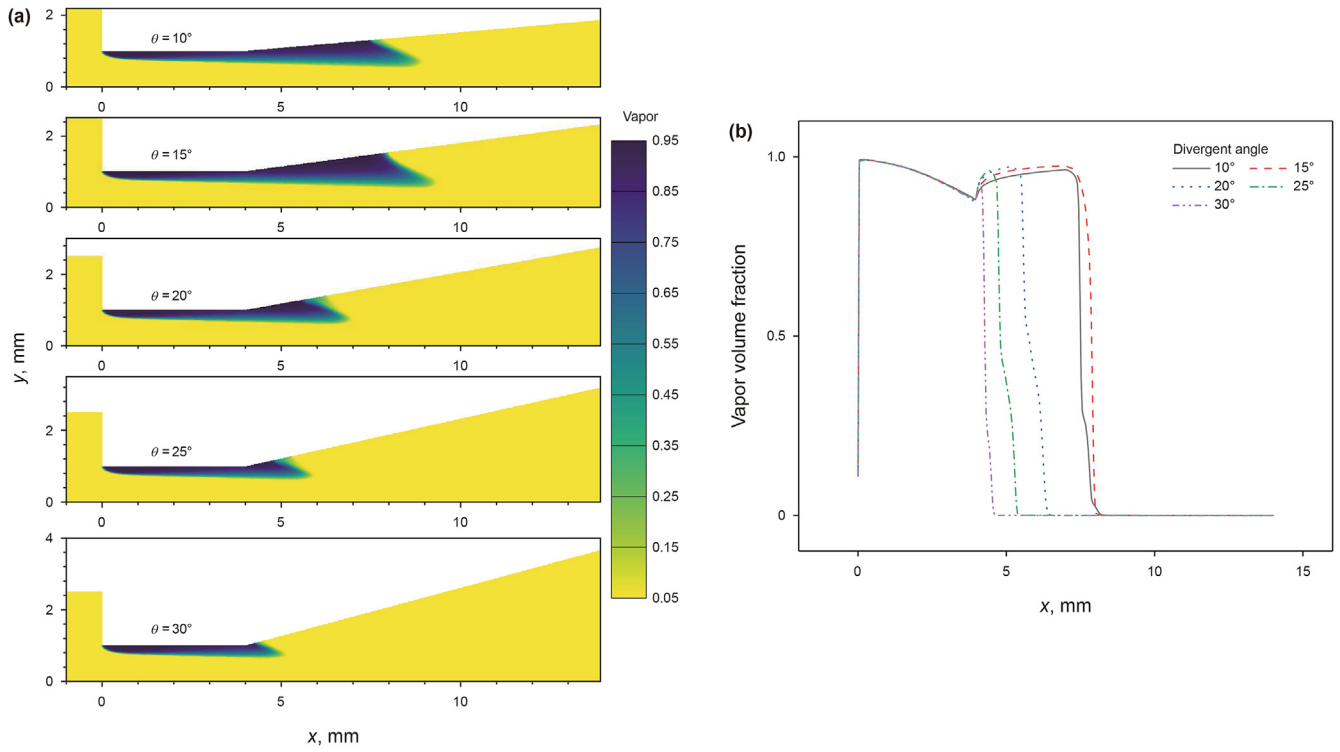

Fig. 8. A comparison of flow field cavitation characteristics. (**a**) Cavitation cloud distribution; (**b**) Vapor volume fraction at walls of nozzle throat and divergent section.

Fig. 11a shows the distribution of cavitation clouds at different throat lengths (L_1). It can be seen that as the L_1 increases gradually, the distribution range of cavitation clouds is enlarged under the entrainment force of jet. While the collapse of cavitation clouds occurs before arriving to divergent section due to the compression of positive pressure, as shown in Fig. 10a. Additionally, the end of cavitation clouds also collapses violently with the increase of L_1. The vapor volume fraction at walls of throat and divergent section is displayed in Fig. 11b. It is seen that lengthening the throat will exacerbate the collapse of cavitation in the process of migration. Though the vapor volume fraction rises op again in the divergent section because of the shear effect, its maximum value drops gradually as L_1 increases.

4.3. Influence of divergent length on flow field

Fig. 12a shows the axial pressure distribution at different divergent lengths (L_2). When L_2 varies from 1d to 3d, it can be seen that maximum negative pressure increases obviously. When L_2 exceeds 3d, the growth rate of maximum negative pressure drops. Fig. 12b presents the velocity distribution at different L_2. The jet potential core generates when L_2 varies from 1d to 3d, and under this condition the cavitation clouds tend to be transported farther. Fig. 13 shows the distribution of cavitation clouds at different L_2. It is easily seen that when $L_2 = 1d$, the area of cavitation clouds is small and the vapor volume fraction is much less than other nozzles. By referring to Fig. 12a, it is found the axial pressure of $L_2 = 1d$ is positive and not conducive to the cavitation inception. Additionally, combining with Fig. 12b, it also indicates that negative pressure plays a dominant role in cavitation generation and the jet potential core provides supporting effect. Finally, according to the contours in Fig. 13, the nozzles with $L_2 = 3d$ generates greatest cavitation clouds and shows potential cavitation erosion ability.

5. Erosion ability test

5.1. Experimental apparatus and procedure

In current study, the visual experimental apparatus for gas hydrate formation and cavitating jet erosion designed by Zhang et al. (2020) was employed to test the erosion ability of OPCJ nozzle. As shown in Fig. 14, the experimental apparatus is mainly composed of a vacuum system, a gas injection system, a water injection system, a data acquisition and processing system, a temperature control system, a water jet system, a visualization reaction vessel, a back pressure system, a methane cylinder, and a cryogenic water tank. The maximum working pressure of the visualization reaction vessel is 20 MPa, and the pressure sensor is located in the upper part of the reaction vessel cover. The vessel is equipped with four ϕ100 mm borosilicate glass windows to achieve the visualization of erosion process. The temperature control system belongs to an air bath, with a temperature range of −20 to 100 °C, and the accuracy is ±0.1 °C. The temperature sensor installed on the upper cover of reactor and monitors the temperature during hydrate formation. A methane cylinder is used to provide methane gas for hydrate formation, and a vacuum system is employed to extract the air in the pipelines and reaction vessel. The pressure, temperature, and methane injected in the vessel are recorded in real time by the data acquisition system. The key component of the water injection system is a double-cylinder fluid infusion pump with a maximum injection pressure of 40 MPa. The water jet system mainly consists of a reciprocating piston pump with a maximum displacement of 6 L/min, a life system used to adjust the standoff distance (the distance between nozzle and target), and varied nozzles. In the actual hydrate drilling and mining process using water jet, the working fluid (water) is transported from the platform to the hydrate layer. The temperature of water is close to that of hydrate reservoir due to cooling or heating effect of seafloor conditions.

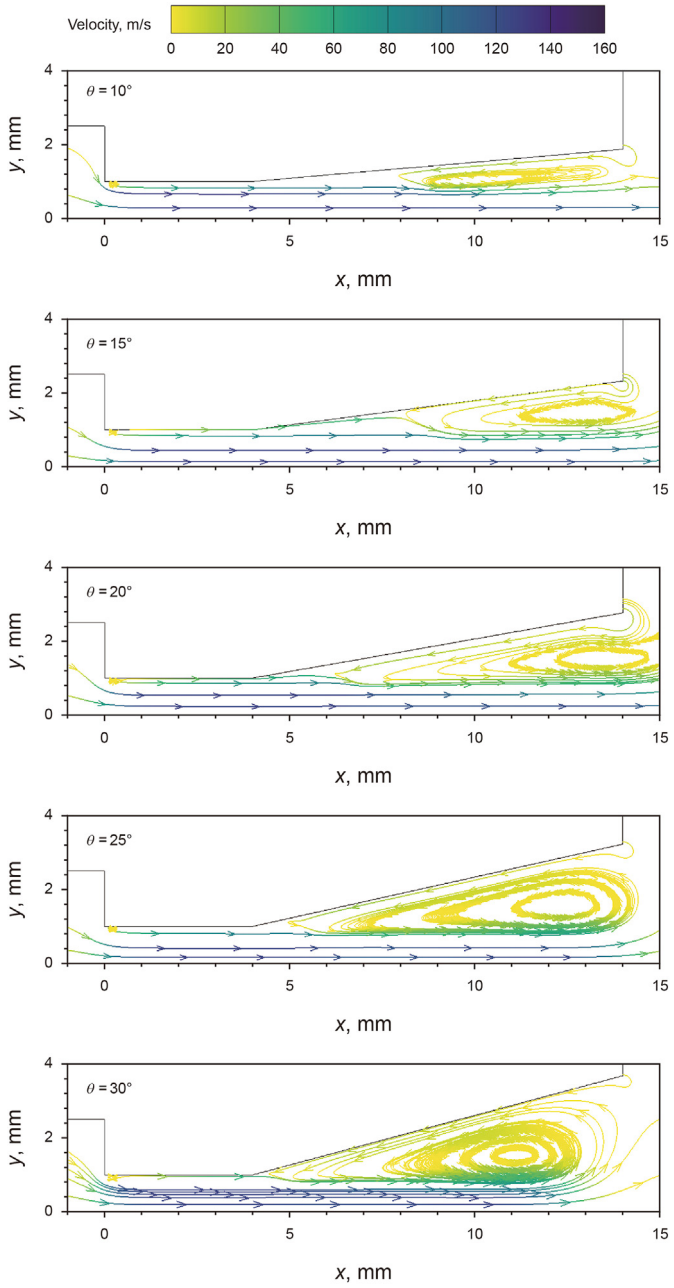

Fig. 9. A comparison of path lines distribution with divergent angles varying from 10° to 30°.

Additionally, the hydrate shows strong temperature sensibility, and the water jet with relatively high temperature can induce thermal stress damage besides jet impact. Therefore, to be consistent with the actual operation conditions and eliminate the influence of thermal effect, the cryogenic water tank is adopted here to provide cryogenic water for the water injection/jet system. The back pressure system mainly includes a back pressure valve with a maximum working pressure of 40 MPa, a manual pump and a wet type gas flowmeter to record the methane gas not involved in hydrate formation. Based this, the volume of methane consumed in the hydrate formation stage can be obtained by calculating the difference between the volume injected and discharged.

In current investigation, the quartz sand is employed as the host sediments. The grain size distribution of the host sand is displayed in Fig. 15 (Li et al., 2018). During the experiment of water jet erosion on GHBS, it is necessary to observe the moving state of sands through the visual window. The fine dust in sands inevitably dissolves in water and make the water turbid, which seriously decrease the visibility of the experiment. The coarse sands may scratch the visual window and lead to issues for long-term observation. Therefore, in present experiments, the sands with the cumulative frequency of 25%–75% are selected and the corresponding sand size is varied from 0.0625 to 0.25 mm. The porosity and median diameter are 40% and 0.1122 mm, respectively.

Meanwhile, a stainless-steel mould with dimensions of 100 mm in diameter and 250 mm in height is prepared for the host sediments. The Ghiassian method proposed by Ghiassian and Grozic (2013) is employed here to calculate the hydrate saturation of the sample. It is assumed that one unit volume methane hydrate will generate 164-unit volume of methane gas and 0.87-unit volume of water. The calculation principle of hydrate saturation is shown in Eq. (14),

$$S_h = \frac{V_h}{V_p} \times 100\% \tag{11}$$

where S_h is the hydrate saturation; V_h is the volume of gas hydrate; and V_p is the volume of pores.

The experimental procedures are as follows:

(1) In present experiments, the designed hydrate saturation of GHBS samples synthesized was 50%. According to the predetermined saturation, the mass ratio of water to sand was calculated as 1:9. Then, dried sand and distilled water were weighed, and fully mixed and stirred. Next, water-based sediments were added to the stainless-steel mould (100 mm for inner diameter and 250 mm for height) several times and tamped.

(2) Open the gas inlet valve and inject methane gas into the reaction vessel to a pressure of 10 MPa. As the data acquisition system recorded, the pressure drop within 10 h was less than 0.1 MPa at room temperature. This indicates a good seal of the vessel, and the air tightness of the device is considered to meet the experimental requirements.

(3) Insert the stainless-steel mould with water-based sediments into the reaction vessel. The vacuum pump was employed to extract the air in the pipelines and vessel to avoid the influence of air on hydrate formation. Then, open the gas inlet valve and inject methane gas into the reaction vessel slowly to a target pressure of 9.5 MPa, then maintain this pressure state for 10 h to make the fully contact with water.

(4) The temperature control system (air bath) was opened and set to 2 °C to synthesize hydrate. When the temperature and pressure in the vessel become stable, the water in the pores is considered to be completely converted into hydrate completely.

(5) The water injection system was opened and cryogenic water (2 °C) was slowly injected into the vessel to displace the free methane and form a submerged water environment. Meanwhile, the manual pump was set to 8 MPa to avoid hydrate decomposition, and the wet type gas flowmeter was employed to record the amount of methane displaced.

(6) Set the back pressure to 5 MPa and adjust the standoff distance to target value. Then open the water jet system and the formed GHBS samples were impinged by varied nozzles. Afterwards, methane gas was injected into the vessel again to a pressure of 9.5 MPa, and the cryogenic water inside was displaced at the same time. This pressure state was

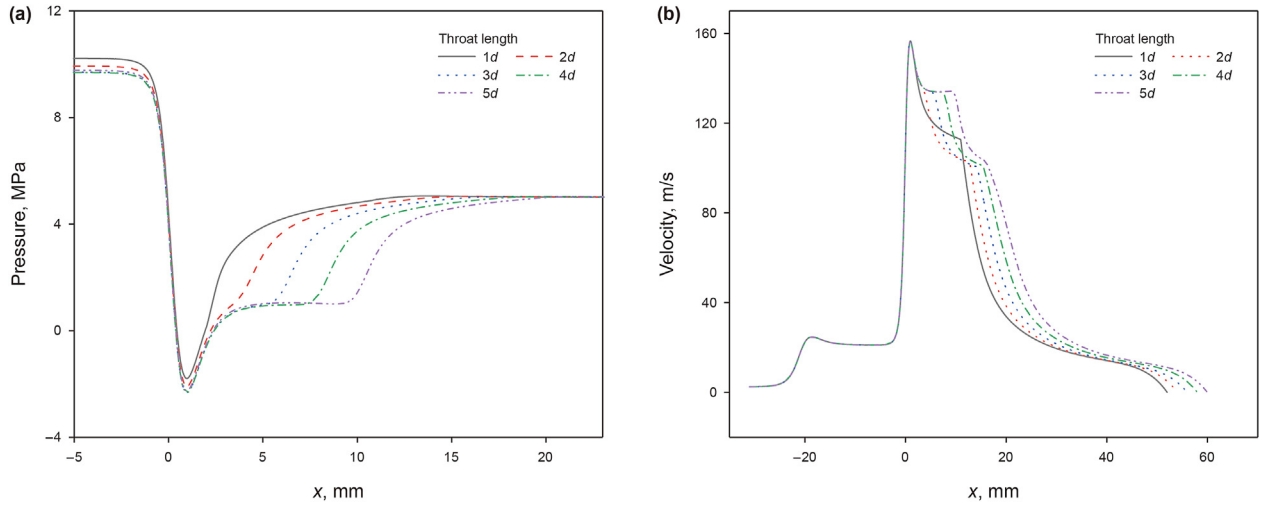

Fig. 10. A comparison of axial flow field characteristics. (**a**) Pressure distribution; (**b**) Velocity distribution.

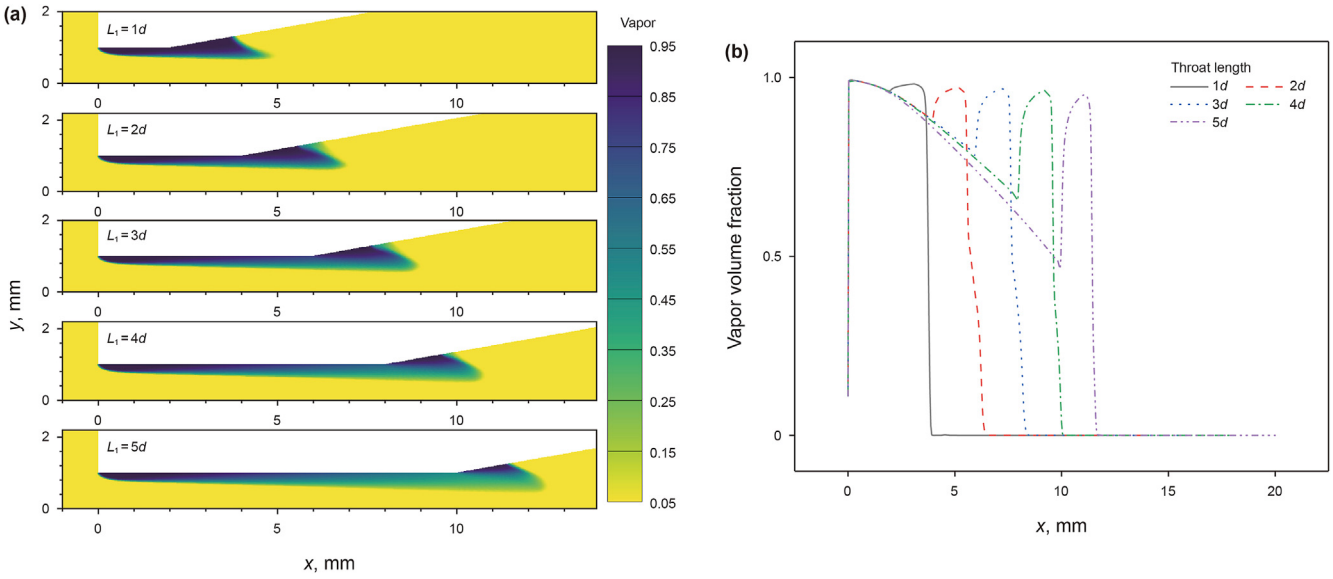

Fig. 11. A comparison of flow field cavitation characteristics. (**a**) Cavitation cloud distribution; (**b**) Vapor volume fraction at walls of nozzle throat and divergent section.

maintained for 12 h, and this step was designed for retaining the morphology of erosion pits.

(7) Discharge methane gas inside the vessel and take out the stainless-steel mould to record the morphological data of erosion pits.

In current study, three groups of repeatability tests were performed using OPCJ and CJ, respectively. The test scheme is presented in Table 2. Here, for OPCJ nozzle, the specifications of resonator structure are followed previous work (Li and Shen, 1987, 1992) and the outlet structure parameters are consistent with the optimization results shown in Section 4. For CJ nozzle, the D_s, d, and α represent the inlet diameter, throat diameter, and conical angle of the CJ nozzle, respectively. The hydraulic conditions are the same for two jets.

5.2. Synthetic process of GHBS

Fig. 16 shows the characteristics of pressure and temperature changes during hydrate formation and combustion test. From Fig. 16a, it can be seen that the hydrate formation process can be divided into four stages according to the pressure and temperature variations: S_1, the temperature and pressure drop stage; S_2, the rapid hydrate formation stage or temperature rise stage; S_3, the slow hydrate formation stage; S_4, hydrate formation completion stage. In S_1, the pressure dropped gradually due to the temperature decrease in the vessel. In S_2, the pressure and temperature in the vessel met the formation conditions of hydrate. Meanwhile, the high pressure of vessel as the driving force increased the formation rate of hydrate, so that the pressure decreased more rapidly in this stage. Additionally, the temperature in the vessel increased slightly, which is against the cooling effect of the temperature control system. That's because the hydrate formation is an exothermic process, and the temperature increase also indicated that hydrates were forming in large quantities. In S_3, the temperature decreased gradually and the temperature dropped slowly due to the cooling effect of air bath. This shows that the formation rate of hydrate decreased gradually. In S_4, pressure and temperature became stable

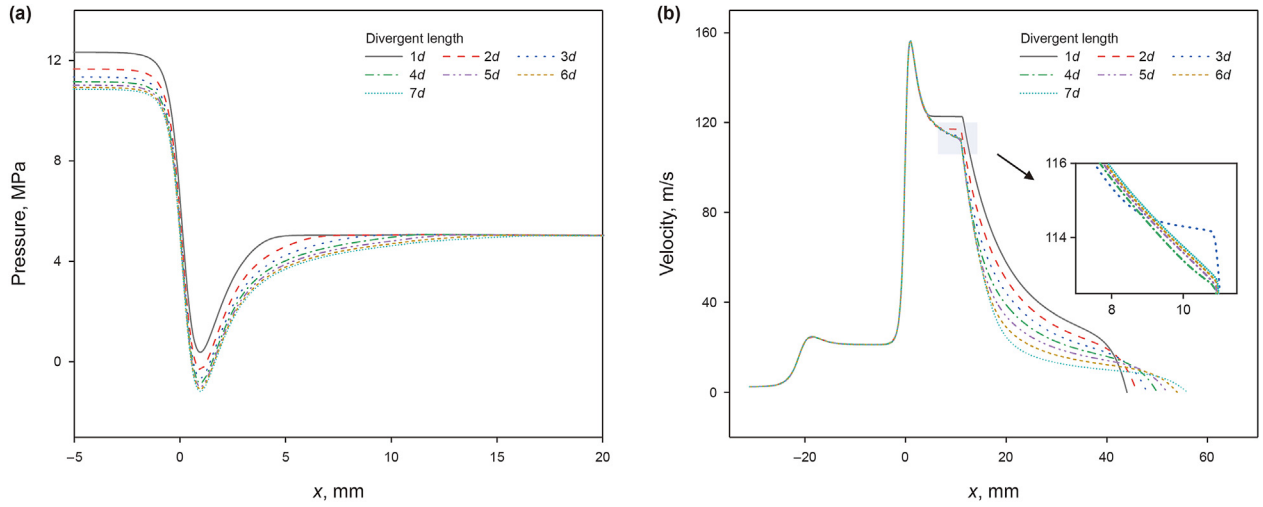

Fig. 12. A comparison of axial flow field characteristics. (**a**) Pressure distribution; (**b**) Velocity distribution.

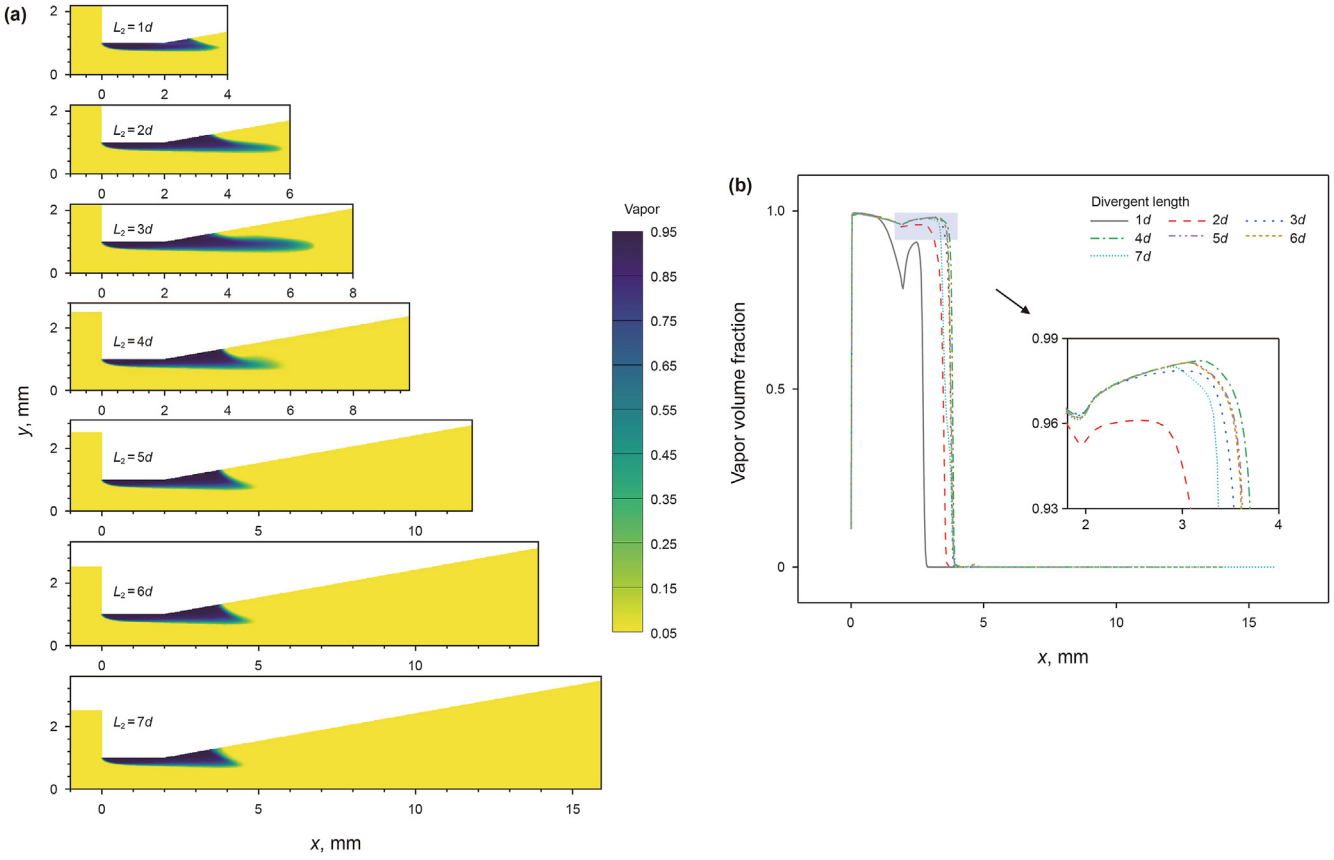

Fig. 13. A comparison of flow field cavitation characteristics. (**a**) Cavitation cloud distribution; (**b**) Vapor volume fraction at walls of nozzle throat and divergent section.

and the hydrate formation rate was quite slow. The synthetic process described above is also consistent with Zhang's experimental results (Zhang et al., 2022a).

According to recorded data of methane gas volume, the difference between injected and displaced methane gas is 69 L. According to the Ghiassian method introduced in Section 5.1, 64.4 L methane is needed in the hydrate formation process of current study. Considering that the residual gas and temperature change in the pipelines and sediments pores, we suppose the distilled water used has been completely converted into hydrate. Moreover, the synthesized GHBS are taken out from the vessel for combustion as shown in Fig. 16b. The sample burns violently with blue flames in the air, indicating that methane gas is continuously released because of hydrate decomposition.

5.3. Erosion results and analyses

The morphology of erosion pits broken by OPCJ and CJ was

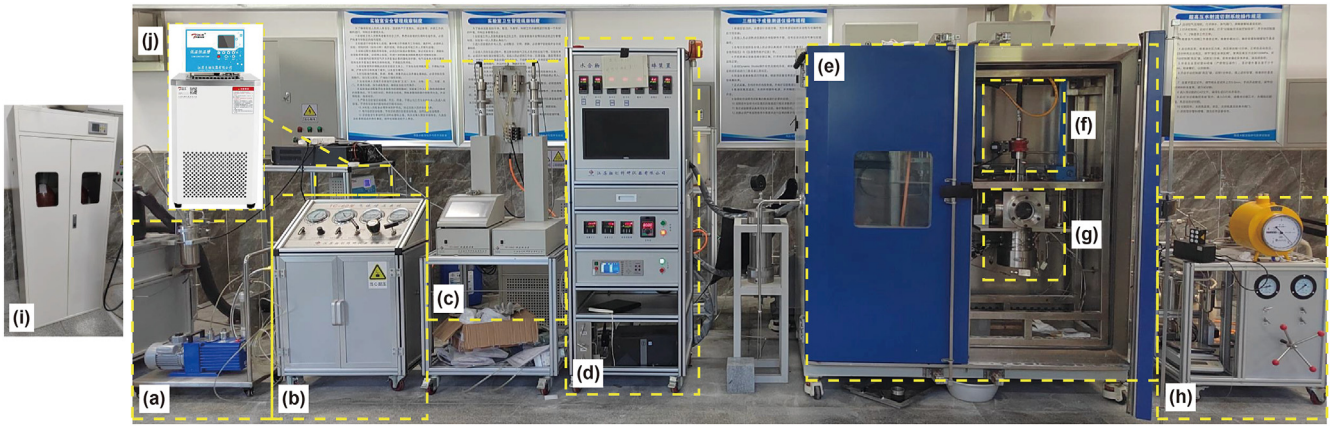

Fig. 14. Visual experimental apparatus for gas hydrate formation and cavitating jet erosion. (**a**) Vacuum system; (**b**) Gas injection system; (**c**) Water injection system; (**d**) Data acquisition and processing system; (**e**) Temperature control system; (**f**) Water jet system; (**g**) Visualization reaction vessel; (**h**) Back pressure system; (**i**) Methane cylinder; (**j**) Cryogenic water tank.

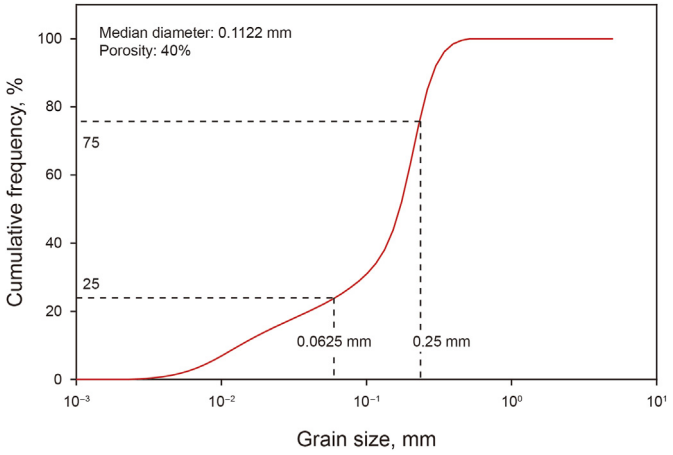

Fig. 15. The grain size distributions of the host sands (Li et al., 2018).

shown in Fig. 17. It can be seen that the section shapes (blue lines) of all tested samples show bilaterally symmetrical, and are similarly fusiform. With the increase of erosion pits depth, the erosion pits diameter increases gradually and then decreases. There exists a maximum breaking diameter for OPCJ and CJ. In contrast to CJ, the diameters of erosion pits induced by OPCJ are larger, which indicates that OPCJ has stronger chambering effect on erosion pits. Moreover, the surfaces of erosion pits in Fig. 17a are all smoother than that in Fig. 17b. It shows that OPCJ has stronger scouring effect on erosion pits and is conducive to bottom hole cleaning to some degree.

Based the erosion pits data, four quantifiable indicators, namely volume erosion rate $\dot{V}$, specific energy E_s, depth erosion rate $\dot{H}$ and specific cutting energy E_{sc} are adopted here to quantitatively characterize and compare the erosion effects of two jets. The calculation principles of these four variables are as follows: $\dot{V}$ is defined as the ratio of erosion pit volume to corresponding erosion time; E_s is defined as the radio of jet energy consumed to the corresponding erosion pit volume; $\dot{H}$ is defined as the radio of erosion pit depth to corresponding erosion time; E_{sc} is defined as the ratio of jet energy consumed to the corresponding erosion time. The formulas are as follows,

$$\left.\begin{aligned} \dot{V} &= V/t \\ E_s &= E/V \\ \dot{H} &= H/t \\ E_{sc} &= E/H \\ E &= \Delta pQt \end{aligned}\right\} \tag{12}$$

where V is the volume of erosion pit; t is the erosion time; E is the jet energy consumed; H is the depth of erosion pit; Δp is the difference between inlet pressure and back pressure; Q is the inlet displacement. Here, V is represented by the volume of host sand that erosion pit can hold. The host sand employed here is consistent with that shown in Fig. 15 and its porosity is 40%. The density of quartz sand is known as 2.65×10^3 kg/m^3 and the density of host sand is calculated to be $2.65 \times 10^3 \times (100\%-40\%)$ kg/m^3. Next, the erosion pit volume is obtained through dividing the weight of hose sand by its density.

The comparison of $\dot{V}$, E_s, $\dot{H}$ and E_{sc} between OPCJ and CJ is presented in Fig. 18. The left vertical axis represents the variable and the right vertical axis represents the mean value of the three groups of experiments for corresponding variable. From Fig. 18a and b, for

Table 2
Jet erosion test scheme.

Geometry of OPCJ nozzle									
D_s, mm	D, mm	L, mm	d, mm	θ, degree	L_1/d	L_2/d	$(D_s/D)^2$	$(D/d)^2$	L/d
6.5	2.5	10.5	1	15	1	3	6.76	6.25	10.50
Geometry of CJ nozzle			Hydraulic parameters						
D_s, mm	d, mm	α, degree	Inlet displacement, L/s		Back pressure, MPa		Standoff distance, mm		Impinged time, s
6.5	1	60	0.085		5		5		60

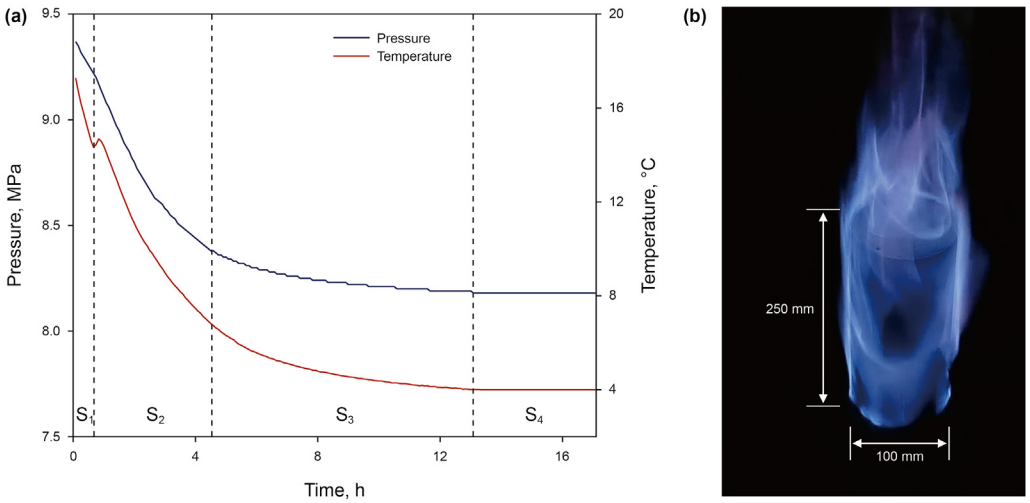

Fig. 16. Generation process of GHBS. (**a**) Pressure and temperature changes during hydrate formation. S_1: the temperature and pressure drop stage; S_2: the rapid hydrate formation stage (temperature rise stage); S_3: the slow hydrate formation stage; S_4: hydrate formation completion stage. (**b**) GHBS with blue flames.

GHBS, the $\dot{V}$ of OPCJ is 1.85 times than that of CJ for GHBS, and the E_s of OPCJ is 0.62 times than that of CJ in present experimental conditions. It can be seen that the OPCJ possesses advantages of high efficiency and low energy consumption. From Fig. 18c, the $\dot{H}$ of OPCJ increases by 15% compared to that of CJ, indicating OPCJ has stronger penetrating effect and higher penetration efficiency on GHBS. Different from $\dot{H}$, E_{sc} is a measurement index of jet penetration ability. In Fig. 18d, CJ has a slight increase of 0.6% in E_{sc} compared to OPCJ, which indicates that OPCJ and CJ have equivalent penetration ability on GHBS.

To explain the superiority of OPCJ in erosion effect on GHBS, the jet impinging models of OPCJ and CJ are established. The hydraulic and nozzle geometry parameters are consistent with the settings in experiments. Fig. 19 shows the comparison of cavitation cloud distribution between OPCJ and CJ. It can be seen that in the flow field of OPCJ, the cavitation clouds are located in the throat and divergent section, while in the CJ fluid domain, there barely exists cavitation characteristics. It indicates that OPCJ has stronger cavitation erosion effect compared to CJ, and can improve the erosion

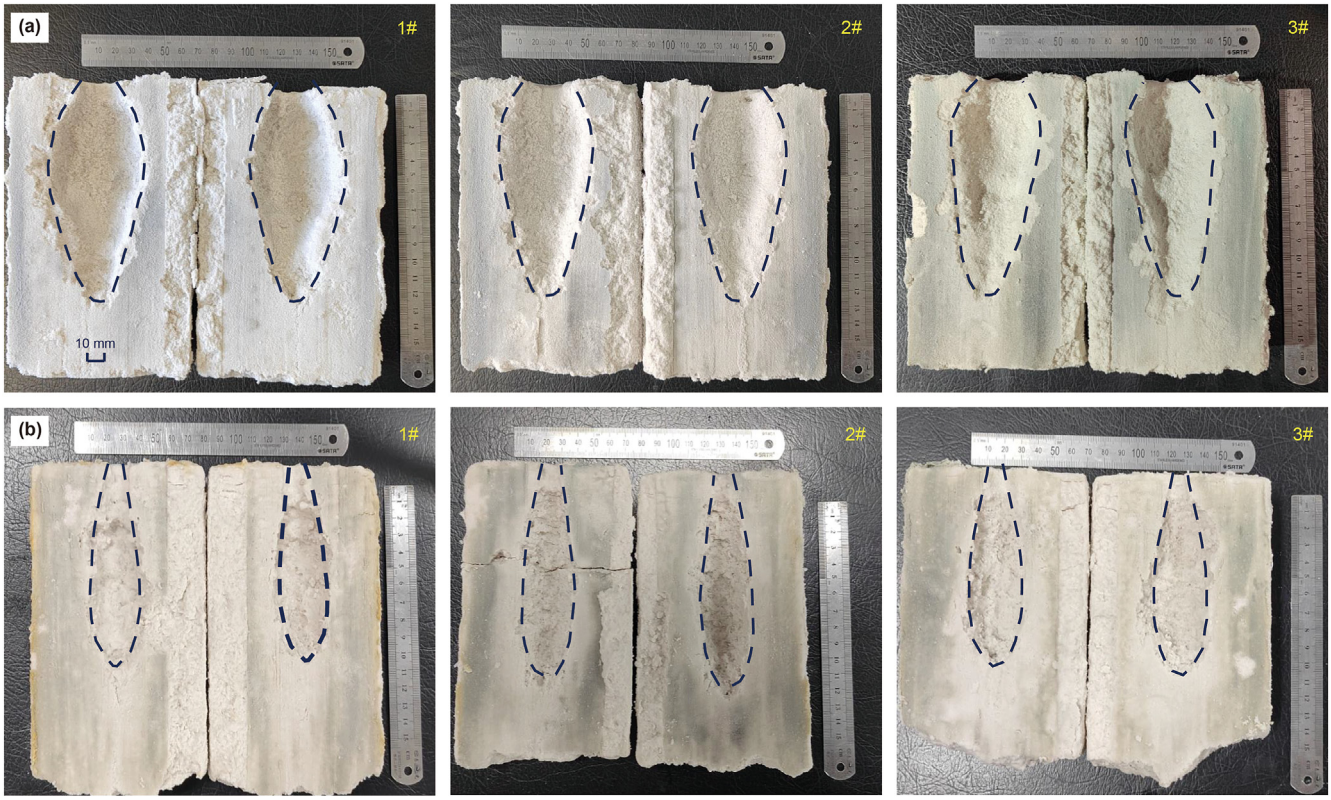

Fig. 17. Erosion pits induced by OPCJ (**a**) and CJ (**b**).

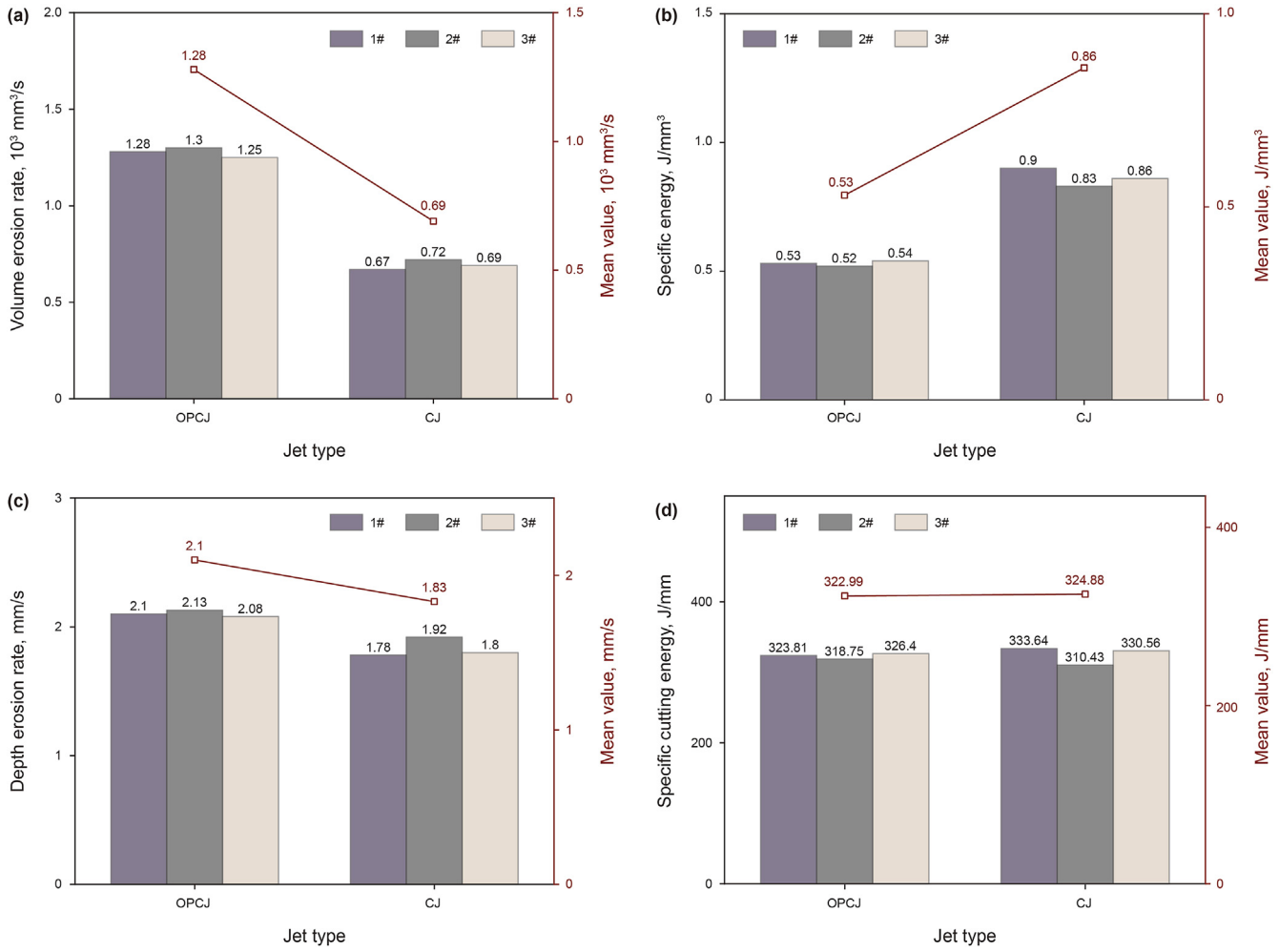

Fig. 18. The comparison of erosion pits data between OPCJ and CJ. (**a**) Volume erosion rate; (**b**) Specific energy; (**c**) Depth erosion rate; (**d**) Specific cutting energy.

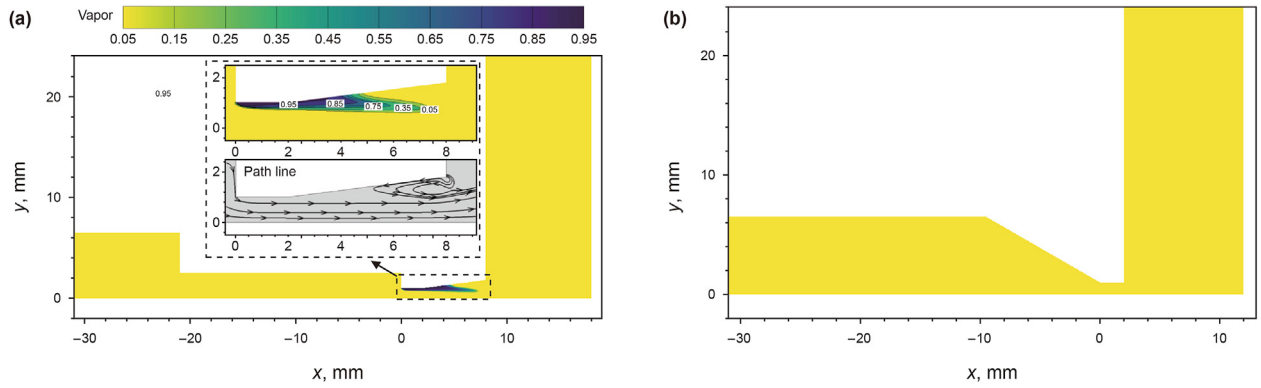

Fig. 19. The comparison of cavitation cloud distribution characteristics between OPCJ (**a**) and CJ (**b**).

efficiency. Fig. 20 presents the pressure, turbulent kinetic energy (TKE) and radial velocity distribution near the impinging wall of OPCJ and CJ models. From Fig. 20a, the maximum value of impinging pressure that OPCJ induces is greater than that of CJ, and it is conducive to generating stronger erosion effect in the depth direction. TKE, as a measure of intensity of turbulence, is one of the most important parameters depending on the momentum transport of fluid. From Fig. 20b, the TKE of OPCJ has an obvious increase than that of CJ, indicating OPCJ is much more unstable during jet impingement. And the strong turbulence intensity helps OPCJ induce violent impact stress in the impinged GHBS. In actual drilling conditions, during the erosion process of water jet on GHBS, the sediments matrix is destroyed and delaminated skeleton sand is easily retained in the erosion pits. From Fig. 20c, it can be seen

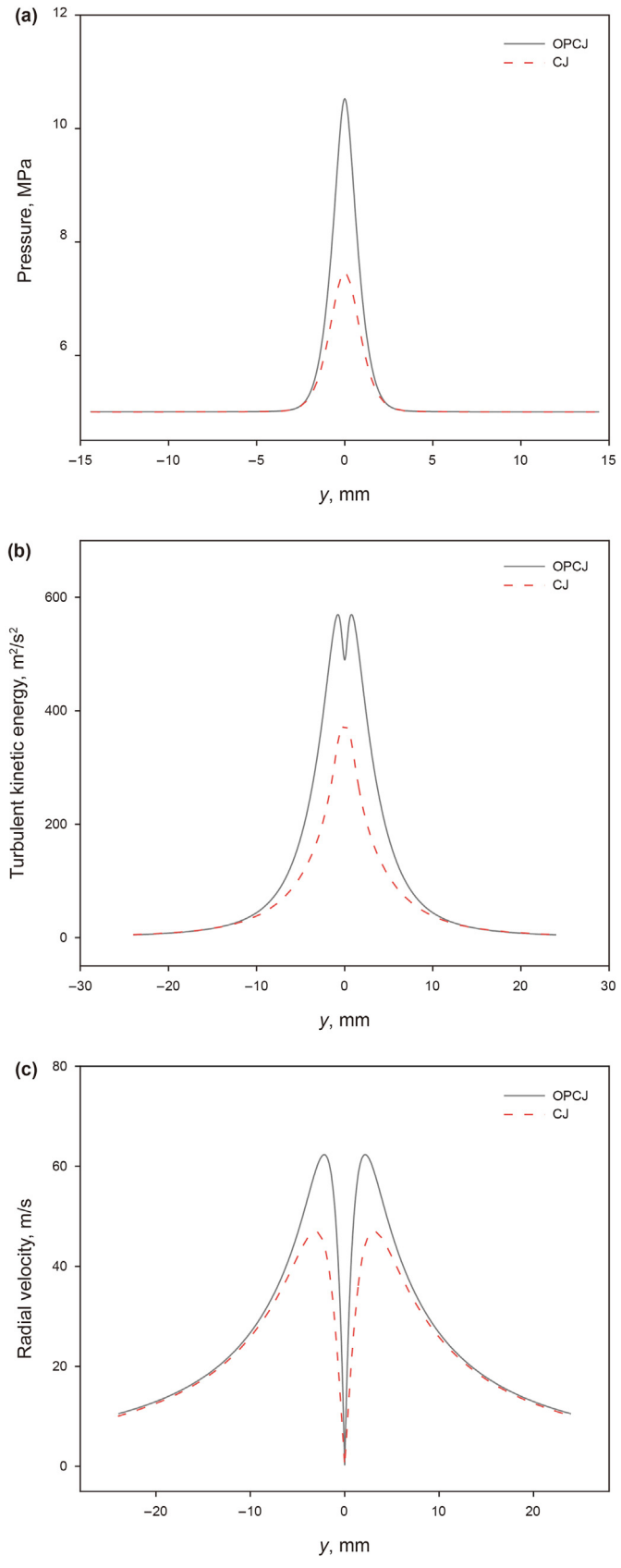

Fig. 20. The comparison of impact characteristics between OPCJ and CJ. (**a**) Pressure along the impact wall; (**b**) Turbulent kinetic energy along the line 0.1 mm away from the impact wall; (**c**) Radial velocity along the line 0.1 mm away from the impact wall.

that OPCJ has larger radial velocity, which illustrates that OPCJ has stronger radial turbulence effect and is more conducive to chambering, sand migration and bottom hole cleaning, as shown in Fig. 17.

6. Conclusions

In present study, we analyse the influences of divergent angle, throat length and divergent angle on the pressure, velocity and cavitation characteristics for the OPCJ flow field. Laboratory experiments of GHBS formation and erosion tests by the OPCJ and CJ are carried out to validate the erosion performance. The impinging models of OPCJ and CJ are also constructed to illustrate the erosion superiority of OPCJ on GHBS. Main conclusions are summarized as follows:

(1) In present simulation conditions, the preferred values of divergent angle, throat length and divergent length are 15°, 1*d*, and 3*d*, respectively, to improve the cavitation erosion effect of OPCJ.
(2) The OPCJ possesses advantages of high efficiency and low energy consumption. In the same hydraulic conditions, for GHBS, the volume erosion rate of OPCJ is 1.85 times than that of CJ, and the specific energy of OPCJ is 0.62 times than that of CJ in present experimental conditions.
(3) For GHBS, the OPCJ has higher penetration efficiency, and shows equivalent penetration ability compared to CJ. The depth erosion rate of OPCJ is 1.15 times than that of CJ, and the specific cutting energy of OPCJ has a slight decrease compared to CJ.
(4) During the impinging process, the OPCJ can induce stronger impact pressure and turbulence effect on GHBS compared to CJ. In the radial direction of erosion pit, the OPCJ shows stronger chambering effect and bottom cleaning ability.

Disclosure statement

No potential conflict of interest was reported by the authors.

Acknowledgements

This work was financially supported by National Natural Science Foundation of China (No. 52174009 and No. 51827804) and Marine Economy Development Foundation of Guangdong Province (GDNRC[2022]44) “Technical Support for Stimulation and Testing of Gas Hydrate Reservoirs”.

References

Brennen, C.E., 2013. Cavitation and Bubble Dynamics. Cambridge University Press.
Cao, M.M., Meng, C., Sun, Y.Z., Wang, H., 2017. Improved design and simulation analysis of a cleaning nozzle. Manuf. Autom. 39 (3), 100–105 (in Chinese).
Celik, F., Ozden, Y.A., Bal, S., 2014. Numerical simulation of the flow around two-dimensional partially cavitating hydrofoils. J. Mar. Sci. Appl. 13 (3), 245–254. https://doi.org/10.1007/s11804-014-1254-x.
Chen, C., Pan, D.B., Yang, L., et al., 2019a. Investigation into the water jet erosion efficiency of hydrate-bearing sediments based on the arbitrary Lagrangian-Eulerian method. Appl. Sci.-Basel. 9 (1), 18. https://doi.org/10.3390/app9010182.
Chen, Y., Li, J., Gong, Z.X., Chen, X., Lu, C.J., 2018. Large eddy simulation and investigation on the laminar-turbulent transition and turbulence-cavitation interaction in the cavitating flow around hydrofoil. Int. J. Multiphas. Flow 112, 300–322. https://doi.org/10.1016/j.ijmultiphaseflow.2018.10.012.
Chen, Y.Z., Hu, Y.H., Zhang, S.L., 2019b. Structure optimization of submerged water jet cavitating nozzle with a hybrid algorithm. Eng. Appl. Comput. Fluid Mech. 13 (1), 591–608. https://doi.org/10.1080/19942060.2019.1628106.
Circone, S., Stern, L.A., Kirby, S.H., et al., 2000. Methane hydrate dissociation rates at 0.1 MPa and temperatures above 272 K. In: Holder, G.D., Bishnoi, P.R. (Eds.), Gas

Hydrates: Challenges for the Future. Annals of the New York Academy of Sciences. New York Acad Sciences, New York, pp. 544–555. https://doi.org/10.1111/j.1749-6632.2000.tb06809.x.
Durham, W.B., Stern, L.A., Kirby, S.H., 2003. Ductile flow of methane hydrate. Can. J. Phys. 81 (1–2), 373–380. https://doi.org/10.1139/p03-042.
Ghiassian, H., Grozic, J.L.H., 2013. Strength behavior of methane hydrate bearing sand in undrained triaxial testing. Mar. Petrol. Geol. 43, 310–319. https://doi.org/10.1016/j.marpetgeo.2013.01.007.
Kawanami, Y., Kato, H., Yamaguchi, H., et al., 1997. Mechanism and control of cloud cavitation. J. Fluid Eng. 119 (4), 788–794. https://doi.org/10.1115/1.2819499.
Lei, C.C., Deng, S.S., Guan, J.F., et al., 2015. Flow field numerical simulation and erosion experiment research of submerged cavitating water jets. J. Chongqing Univ.Technol. (Nat. Sci.). 29 (12), 71–76 (in Chinese).
Li, D.L., Wu, Q., Wang, Z., et al., 2018. Tri-axial shear tests on hydrate-bearing sediments during hydrate dissociation with depressurization. Energies 11 (7), 12. https://doi.org/10.3390/en11071819.
Li, G.S., Tian, S.C., Zhang, Y.Q., 2020. Research progress on key technologies of natural gas hydrate exploitation by cavitation jet drilling of radial wells. Petrol. Sci. Bull. (3), 349–365 (in Chinese).
Li, G.S., Shen, Z.H., 1987. Rock cutting effect with self-resonanting cavitation jets under atmospheric pressure. J. Univ. Pet., China (Ed. Nat. Sci.) (3), 12–22 (in Chinese).
Li, G.S., Shen, Z.H., 1992. Design principle of organ-pipe cavitating jet nozzles. J. Univ. Pet., China. 16 (5), 35–39 (in Chinese).
Li, H., Kelecy, F.J., Egelja-Maruszewski, A., Vasquez, S.A., 2008. Advanced computational modeling of steady and unsteady cavitating flows. In: ASME 2008 International Mechanical Engineering Congress and Exposition. https://doi.org/10.1115/IMECE2008-67450.
Liang, H.Y., Guan, D.W., Shi, K.J., et al., 2022. Characterizing mass-transfer mechanism during gas hydrate formation from water droplets. Chem. Eng. J. 428, 132626. https://doi.org/10.1016/j.cej.2021.132626.
Liao, H.L., Zhao, S.L., Cao, Y.F., et al., 2020. Erosion characteristics and mechanism of the self-resonating cavitating jet impacting aluminum specimens under the confining pressure conditions. J. Hydrodyn. 32 (2), 375–384. https://doi.org/10.1007/s42241-020-0024-2.
Liao, H.L., Wang, E.C., Dong, L., et al., 2022. Test on abrasive jet cutting features of simulated hydrate reservoir. J. Cent. S. Univ. 53 (3), 924–932 (in Chinese).
Liu, H.L., Liu, D.X., Wang, Y., et al., 2013. Application of modified k-ω model to predicting cavitating flow in centrifugal pump. Water Sci. Eng. 6 (3), 331–339. https://doi.org/10.3882/j.issn.1674-2370.2013.03.009.
Mathieu, C., Pierre, F.J., Marie, M.J., Michel, R., 2001. The cavitation instability induced by the development of a re-entrant jet. J. Fluid Mech. 444, 223–256. https://doi.org/10.1017/S0022112001005420.
Pang, X.Q., Jia, C.Z., Chen, Z.X., et al., 2022. Reduction of global natural gas hydrate (NGH) resource estimation and implications for the NGH development in the South China Sea. Petrol. Sci. 19 (1), 3–12. https://doi.org/10.1016/j.petsci.2021.12.006.
Plesset, M.S., 1949. The dynamics of cavitation bubbles. J. Appl. Mech. 16 (3), 277–282. https://doi.org/10.1115/1.4009975.
Rayleigh, L., 1917. VIII. On the pressure developed in a liquid during the collapse of a spherical cavity. Lond. Edinb. Dublin. Phil. Mag. J. Sci. 34 (200), 94–98. https://doi.org/10.1080/14786440808635681.
Schnerr, G.H., Sauer, J., 2001. Physical and numerical modeling of unsteady cavitation dynamics. In: ICMF-2001, 4th International Conference on Multiphase Flow. New Orleans, USA.
Shen, Z.H., Li, G.S., Wang, Z.M., Xu, Y.J., 1991. New jet theory and prospects of its application in drilling engineering. Phys. Status Solidi 150 (2), 567–574. https://doi.org/10.1002/pssb.2221500234.
Shi, H.B., Li, M.D., Nikrityuk, P., Liu, Q.X., 2019. Experimental and numerical study of cavitation flows in venturi tubes: from CFD to an empirical model. Chem. Eng. Sci. 207, 672–687. https://doi.org/10.1016/j.ces.2019.07.004.
Shi, K.J., Wang, Z.F., Jia, Y.X., et al., 2022. Effects of the vertical heterogeneity on the gas production behavior from hydrate reservoirs simulated by the fine sediments from the South China Sea. Energy 255, 124525. https://doi.org/10.1016/j.energy.2022.124525.
Tan, Y.W., Zhang, Y.Q., Yu, C., et al., 2022. Evolution of the cavitation cloud and stability of flow fields in a cavitating jet. Petrol. Sci. Bull. 7 (1), 71–80 (in Chinese).
Tang, Y., Sun, P., Wang, G.R., et al., 2020. Rock-breaking mechanism and efficiency of straight-swirling mixed nozzle for the nondiagenetic natural gas hydrate in deep-sea shallow. Energy Sci. Eng. 8 (10), 3740–3752. https://doi.org/10.1002/ese3.779.
Terzariol, M., Goldsztein, G., Santamarina, J.C., 2017. Maximum recoverable gas from hydrate bearing sediments by depressurization. Energy 141, 1622–1628. https://doi.org/10.1016/j.energy.2017.11.076.
Thomson, G.W., 1946. The antoine equation for vapor-pressure data. Chem. Rev. 38 (1), 1–39. https://doi.org/10.1021/cr60119a001.
Wang, G.R., Huang, R., Zhong, L., et al., 2018. An optimal design of crushing parameters of Marine gas hydrate reservoirs in solid fluidization exploitation. Nat. Gas. Ind. 38 (10), 84–89. https://doi.org/10.1016/j.ngib.2018.10.006.
Wang, G.R., Zhong, L., Zhou, S.W., et al., 2017. Jet breaking tools for natural gas hydrate exploitation and their support technologies. Nat. Gas. Ind. 37 (12), 68–74. https://doi.org/10.1016/j.ngib.2017.12.011.
Wang, L.Z., Wang, G.R., 2020. Experimental and theoretical study on the critical breaking velocity of marine natural gas hydrate sediments breaking by water jet. Energies 13 (7), 11. https://doi.org/10.3390/en13071725.
Wang, R., Hu, F.J., 2015. ANSYS Workbench Engineering Numerical Analysis Technology and Application Examples. China Railway Publishing House, Beijing (in Chinese).
Wang, Y.W., Huang, C.G., Du, T.Z., et al., 2012. Shedding phenomenon of ventilated partial cavitation around an underwater projectile. Chin. Phys. Lett. 29 (1). https://doi.org/10.1088/0256-307X/29/1/014601.
Wu, X.Y., Zhang, Y.Q., Tan, Y.W., et al., 2022. Flow-visualization and numerical investigation on the optimum design of cavitating jet nozzle. Petrol. Sci. https://doi.org/10.1016/j.petsci.2022.05.016.
Xu, Z., Hu, T., Pang, X.Q., et al., 2022. Research progress and challenges of natural gas hydrate resource evaluation in the South China Sea. Petrol. Sci. 19 (1), 13–25. https://doi.org/10.1016/j.petsci.2021.12.007.
Xue, S.X., 2006. High Pressure Waterjet Technology & Engineering. Hefei University of Technology Press, Anhui (in Chinese).
Yakhot, V., Orszag, S.A., 1986. Renormalization group analysis of turbulence. I. Basic theory. J. Sci. Comput. 1 (1), 3–51. https://doi.org/10.1007/BF01061452.
Yang, L., 2018. Study on the Breaking Process of Marine Hydrate Subjected to High Pressure Water Jet and the Production Increase of Marine Hydrate Reservoirs Reconstruction. Jilin University, Changchun, China (in Chinese).
Yang, M.J., Fu, Z., Zhao, Y.C., et al., 2016. Effect of depressurization pressure on methane recovery from hydrate-gas-water bearing sediments. Fuel 166, 419–426. https://doi.org/10.1016/j.fuel.2015.10.119.
Yang, P., Wang, G.R., 2019. Numerical simulation of transportation of particles in jet breaking with solid fluidization method. Shipbuild. China. 60 (4), 108–114 (in Chinese).
Yao, L.M., Zhao, Y., Li, D.W., et al., 2014. Numerical research of the environmental influence of different depth on the shape of cavitation jet. Chin. J. Hydrodyn. 29 (6), 675–682 (in Chinese).
Ye, J.L., Qin, X.W., Xie, W.W., et al., 2020. Main progress of the second gas hydrate trial production in the South China Sea. Chin. Geol. 47 (3), 557–568. https://doi.org/10.12029/gc20200301.
Yu, T., Guan, G.Q., Abudula, A., et al., 2019. Gas recovery enhancement from methane hydrate reservoir in the Nankai Trough using vertical wells. Energy 166, 834–844. https://doi.org/10.1016/j.energy.2018.10.155.
Yu, X.Y., Zhong, L., Wang, G.R., et al., 2022. A new model for predicting hydrate breaking depth of single nozzle in solid fluidization exploitation and its verification. Nat. Gas. Ind. 42 (3), 150–158 (in Chinese).
Zhang, G.B., Ma, X.L., Jiang, D.D., et al., 2022a. Characteristics of hydrate formation, decomposition, and phase equilibrium in the transition area formed by the high-pressure jet breaking and sand filling method. Energy Rep. 8, 312–321. https://doi.org/10.1016/j.egyr.2021.11.261.
Zhang, J.C., Zhong, L., Wang, G.R., et al., 2021. Experimental study on crushing law of single jet for non-diagenetic gas hydrate. J. Cent. S. Univ. 52 (2), 607–613 (in Chinese).
Zhang, L.X., Dong, H.S., Dai, S., et al., 2022b. Effects of depressurization on gas production and water performance from excess-gas and excess-water methane hydrate accumulations. Chem. Eng. J. 431, 133223. https://doi.org/10.1016/j.cej.2021.133223.
Zhang, P.P., Zhang, Y.Q., Zhang, W.H., et al., 2022c. Numerical simulation of gas production from natural gas hydrate deposits with multi-branch wells: influence of reservoir properties. Energy 238. https://doi.org/10.1016/j.energy.2021.121738.
Zhang, X.W., Hu, T., Pang, X.Q., et al., 2022d. Evaluation of natural gas hydrate resources in the South China Sea by combining volumetric and trend-analysis methods. Petrol. Sci. 19 (1), 37–47. https://doi.org/10.1016/j.petsci.2021.12.008.
Zhang, Y.Q., Wu, X.Y., Li, G.S., et al., 2022e. Study on erosion performance of swirling cavitating jet for natural gas hydrate. J. Cent. S. Univ. 53 (3), 909–923 (in Chinese).
Zhang, Y.Q., Zhao, K.X., Wu, X.Y., et al., 2020. An innovative experimental apparatus for the analysis of natural gas hydrate erosion process using cavitating jet. Rev. Sci. Instrum. 91 (9), 7. https://doi.org/10.1063/5.0011951.
Zhang, Z.L., Liang, Z.M., Gao, X.S., 2000. Numerical simulation of axisymmetric jet flow field. Chin. Petrol. Mach. 28 (8), 1–3+3 (in Chinese).
Zhou, S.W., Chen, W., Li, Q.P., 2014. The green solid fluidization development principle of natural gas hydrate stored in shallow layers of deep water. China Offshore Oil Gas 26 (5), 1–7 (in Chinese).
Zhou, S.W., Zhao, J.Z., Li, Q.P., et al., 2017. Optimal design of the engineering parameters for the first global trial production of marine natural gas hydrates through solid fluidization. Nat. Gas. Ind. 37 (9), 1–14. https://doi.org/10.1016/j.ngib.2018.01.004.